Adaptation of the PTV method for droplets evaporating in vicinity of a flame

Gaël Parant, Laurent Zimmer, Antoine Renaud, Franck Richecoeur

Noname manuscript No.
(will be inserted by the editor)

Adaptation of a PTV method for droplets evaporating in vicinity of a flame

Gaël Parant*, Laurent Zimmer, Antoine Renaud, Franck Richecoeur

Received: date / Accepted: date

Abstract Measuring the time and length of fuel droplet evaporation provides a better understanding of spray dynamics. When a droplet evaporates, it is increasingly difficult to detect it, and therefore it is difficult to track it with a Particle Tracking Velocimetry (PTV) algorithm. To solve this problem, classical PTV algorithms were adapted by exploiting the image of the droplet at frame N to find it in frame N+1. In addition, Interferometric Laser Imaging Droplet Sizing (ILIDS) was used to measure the droplets' physical size from the images collected for the PTV. This new algorithm was applied to a counter-current burner with dodecane droplets evaporating on an air-methane flame. Particle Image Velocimetry (PIV) was used to measure the air velocity field and the temperature field by Rayleigh measurement. The treatment of the data collected during the experiment shows that the PTV algorithm followed the droplets during all their evaporation phase, which would have been very challenging for a classical PTV algorithm. Moreover, since droplets evaporate in a high-temperature environment, it is impossible to track their physical size from ILIDS obtained with a continuous wave laser source. Therefore the follow-up of the droplet during its all evaporating phase was necessary.

1 Introduction

Droplets and sprays are widely used for material synthesis, liquid fuel injection in internal combustion engines, and other industrial applications. The evaporation length and delay are essential to analyzing mass exchange between the environment and the droplets.

Direct measurement by recording the evaporation of the droplets provides excellent results [1–5]. Even when the droplet evolves in an environment with an inhomogeneous temperature, it is still possible to obtain results with a high degree of accuracy [6]. More advanced non-intrusive techniques, such as Phase Rainbow Refractometry [7–9] or two colors laser-induced fluorescence [10], succeed in tracking the droplet diameter and temperature during the evaporation process. However, these diagnoses quickly reach their limits when the trajectory of the droplets is not known in advance or when the droplets become very small. New strategies must be developed for tiny droplets (a few tens of microns) with arbitrary trajectories.

Interferometric measurements have been used to measure the droplets diameter while tracking their position. This technique, introduced by Konig et al.[11] since then improved upon [12–15] and formalized by Damaschke et al.[16], allows the measurement of the diameter of the droplets by counting the number of interference fringes resulting from the interaction between the laser and the droplets. This technique allowed Park et al.[17] to understand the spatial distribution of the droplets due to simultaneous measurement of their position and diameter. The evaporation of droplets near a flame by Thimothee et al.[18] was measured using this technique, showing its potential as a diagnostic in burnt gases. Wu et al.[19] have taken this diagnostic further by using the fringe position to estimate a nanometric variation of the droplet size. In the limit of a slight

* gael.parant@centralesupelec.fr

EM2C, CNRS, CentraleSupélec, Université Paris Saclay, 3 Rue Joliot-Curie, 91190 Gif-sur-Yvette, France

change in diameter, the number of fringes hardly changes, unlike the position of the fringes, which varies proportionally to the diameter.

When the evaporation occurs in a constrained environment, such as high ambient temperature, the diameter decreases rapidly. Consequently, the number and position of the fringes are not stable, making it impossible to use interferometric measurements. Thus, if ILIDS is created from a continuous wave laser, it is impossible to correctly identify the interference fringes on the camera image because of a significant movement during the exposure time. To measure the time and distance in this type of evaporation, it becomes crucial to follow the droplets during their whole life.

In order to automatically track these droplets during their evaporation, PTV algorithms can be used. Maas et al.[20] were the first to propose an automatic PTV algorithm. To track droplets, classical PTV algorithms perform two steps[21]: droplets are detected on each image, and the trajectories are reconstructed from the detected droplets. Even in more recent work, this structure is retained[22, 23]. Generally, studies to improve PTV algorithms have focused on matching features from one image to another because the particles to be tracked are often identical. However, the light intensity decreases sharply as the diameter decreases[24], and thus finding droplets at the end of their evaporation becomes a challenging task. So it is not possible to correctly identify the tiny droplets when using an intensity trigger as in Lee et al.[25]. To our knowledge, only Thimothee et al.[18] have performed PTV monitoring of evaporating droplets together with an ILIDS measurement to determine their diameter. However, little detail is given about their tracking algorithm and the configuration they used.

We will modify the PTV algorithms to adapt them to, what we call *rapidly* evaporating droplets, blurred during evaporation, coupled with an ILIDS measurement.

During the evaporation phase, the droplets gradually become smaller and less visible. So to correctly follow them during this phase, the current PTV algorithm uses the image of the droplet at frame N to find it at frame N+1. In this way, we will follow the droplet from one step to the next, even when it becomes very faint.

The present work is divided into four parts. The details of the new PTV algorithm is first presented. Then the experimental configuration, in which measurements are performed, is described together with the velocity and temperature field. Results of tracking and evaporation characteristics are then determined. Finally, the effects of burnt gases on the quality of the measurements are discussed.

2 Droplet tracking, diameter measurement and evaporation

2.1 Droplet image and diameter measurement

PTV tracking is a post-processing technique that allows for tracking particles - here droplets - on consecutive images taken with a small time interval. First, a bank of images of the droplets and a set of descriptors of those droplets are injected into the algorithm and then it can follow the trajectories of these particles.

The ILIDS, on the other hand, measures the physical size of the droplets. According to Mie's theory, when a laser illuminates a droplet, the rays of the first-order refraction and the reflection on the droplet interfere with each other. This interference can be measured at a precise angle. Damaschke [16] introduced the following formula to trace the physical size of droplets:

$$N_f = D\frac{\arcsin\left(d_a/2z_l\right)}{\lambda}\left(\cos\left(\frac{\phi}{2}\right)+\frac{n\sin\left(\frac{\phi}{2}\right)}{\sqrt{n^2+1-2n\cos\left(\frac{\phi}{2}\right)}}\right) \tag{1}$$

where N_f is the number of fringes; D is the droplet diameter; d_a is the lens aperture diameter; z_l is the distance from the lens to the light sheet; λ is the light source wavelength; ϕ is the angle of collection relative to the laser sheet; and n is the refractive index of the liquid.

In order to limit the superposition of the droplets on the camera, a particular mask is placed on the camera, which changes the image of droplets image[26]. The fringes of the droplets in the present work are vertical. The PTV algorithm will seek out this pattern. Compared to the classical

compressed ILIDS[14,15], this mask limits the superposition of droplets on the same line while allowing the precise measurement of the apparent diameter. The apparent diameter is a precise measurement of the distance to the focal plane. This mask does not interfere with the number of visible fringes.

The following of this section presents the PTV algorithm in detail and the ILIDS measurement.

2.2 Structure of the PTV algorithm

The PTV algorithm goes through the images collected by the camera to find and track the droplets in each frame. Figure 1 shows how the algorithm works from the droplets found at frame N to find the droplets at frame N+1. First of all, the scheme is detailed, and then the algorithm's initialization is presented.

The *state* of the k-th droplet processed by the algorithm at frame N is noted as D_N^k. The *state* gathers all the data relative to the position and the image of the droplet at a given frame. Thus the set of droplets of frame N, D_N, is defined as $D_N = \left\{D_N^k, k \in \mathbf{N}\right\}$. And the k-th droplet processed by the algorithm, D^k, is defined by $D^k = \left\{D_N^k, N \in \mathbf{N}\right\}$.

The first step of the algorithm consists of searching for the droplets D_N on the frame N+1. The droplets found are called *followed* because they are searched from their image on frame N. The detail of the *follow-up* is presented later.

In the presented example (Figure 1), the droplets D^k and D^{k+1} are found in the frame N+1. The droplets found give the *state* D_{N+1}^k and D_{N+1}^{k+1}. However, the droplet D^{k+2} is not found by the tracking algorithm at frame N+1 and so the algorithm no longer searches this droplet.

The second step consists in *detecting* the droplets of the frame N+1. F_{N+1} is the set of droplets found during the *detection* phase, and F_{N+1} and F_{N+1}^j is the j-th droplet found in the frame N+1. The way droplets are *detected* is detailed below. It happens that droplets are tracked but not detected.

In figure 1, the droplets *detected* are marked with dotted circles. The algorithm detected all three droplets.

The third and last step consists in finding the new droplets among all the detected droplets. These new droplets form the set P_{N+1}. The *state* of these droplets is specified in order to add them to the set D_{N+1}.

In the example of the scheme in figure 1, a new droplet is found. The position, the size, and the image of this droplet are finely determined in order to create the D_{N+1}^{k+3} element. This is the k+3th droplet processed by the algorithm.

Once this step is finished, the algorithm resumes with the set D_{N+1} to search in frame N+2.

The initialization of this algorithm at frame one is simply done by skipping the *follow-up* step because all the droplets present on the image are new.

The *follow-up* phase from one frame to another is not parallelizable. However, this step can be parallelized over all the droplets within a frame. Besides, the *detection* phase can be parallelized on all frames to accelerate the data processing before *follow-up*. The *follow-up* phase is the one that will limit the computation time.

2.3 Droplet *detection* method

The *detection* algorithm is detailed before the *follow-up* because all the *followed-up* droplets are previously *detected*. In order to find the droplets on the image, a simplified image of them is used as a reference (see T_N^k figure 2). The simplified image is a square image with a circle inside centered relative to the image. A radius and a width define the circle. The pixels within the circle are 1, and the others are set to 0. To create a simplified image, the size of the image and the parameters of the circle are required. A cross-correlation algorithm is then applied to find this simplified image on the whole image acquired by the camera. Only the local maxima of this correlation are retained. The simplified images and correlation trigger level are manually calibrated to maximize the number of droplets detected and minimize the false positives. The calibration is done on random images from the image bank to be processed to limit the selection bias. The set of *detected* droplet positions at frame N will form the set P_N.

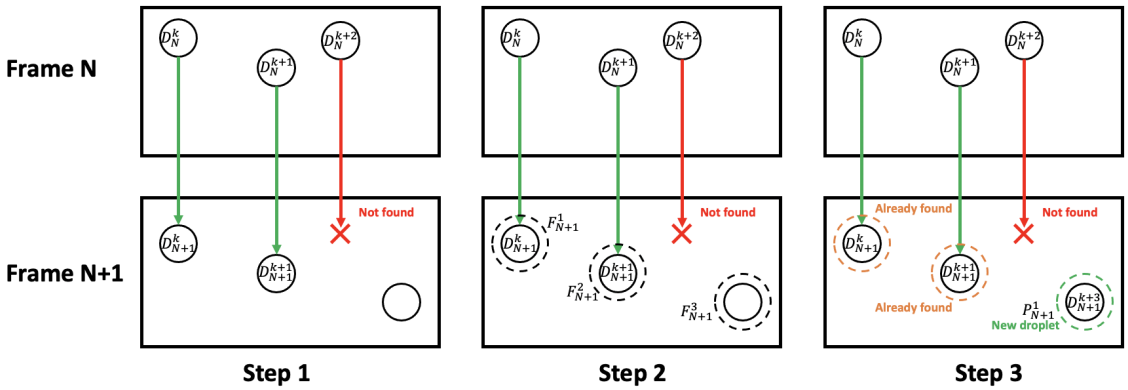

Fig. 1: Diagram illustrating the PTV algorithm from frame N to frame N+1.

2.4 Method of *follow-up* droplets frame by frame

When a new droplet is *detected*, its *status* is specified as follows:

1. A set of simplified images is compared to the droplet to determine the best one, maximizing the correlation between the real and the simplified image (T_N^k in Figure 2) then a 3-point quadratic interpolation is used to determine the apparent radius to sub-pixel accuracy. The best simplified image of a droplet is denoted T_N^k
2. This simplified image is centered with respect to the droplet at a sub-pixel precision thanks to a cross-phase correlation in order to precisely measure its position
3. The effective image of the droplet is obtained by keeping only the signal inside the simplified image ($\tilde{I}_N^k$ on figure 2)

Thus, its position, the best simplified image, its image and its effective image are determined. These elements are included in the *state* of the droplet and thus D_N^k. The I_N^k image and the $\tilde{I}_N^k$ effective image of the droplet are samples of the slightly larger N frame of the image of the droplet, as illustrated in figure 2.

The *follow-up* of the droplet D_k on frame N+1 from D_N^k is done as follows:

1. A sample S_{N+1}^k of the image size of I_N^k and at the same position as D_N^k is taken from frame N+1
2. A phase cross-correlation [27] is performed between S_{N+1}^k and $\tilde{I}_N^k$ to determine the droplet offset between frame N and frame N+1
3. Once the position of the droplet is well determined, its *state* is specified to give D_{N+1}^k, as described above

The droplets only need to be *detected* once to start the *follow-up*. Thus, the *detection* algorithm does not need to find all the droplets on each image; this allows for relaxing the detection criteria and thus limiting the false positives.

2.5 Measurement of the number and position of interference fringes

Once the PTV algorithm is completed, the number and position of the interference fringes is measured. This work is done from the effective images $\tilde{I}_N^k$:

1. $\tilde{I}_N^k$ is vertically averaged to obtain the interference signal
2. A 5th order Butterworth low pass filter is applied to smooth the signal. The filter is applied back and forth so that the initial phase is not modified
3. The signal undergoes a Fourier transform with a zero padding method to improve the accuracy (the signal length is increased 100 times)

The number of fringes is then determined by the spatial mode given by the maximum of the Fourier transform. In addition, the phase associated with this peak is also measured to determine

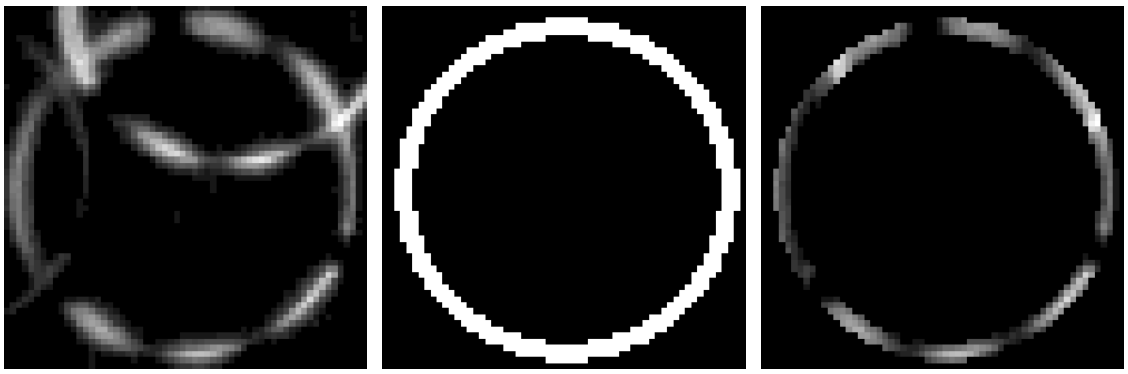

(a) I_N^k (b) T_N^k (c) $\tilde{I}_N^k$

Fig. 2: Example of a fuel droplet image.

the position of the interference fringes. Thus, the position and the number of fringes are entirely determined with precision.

These items can be added to the droplet *status* and done during PTV tracking so that the actual $\tilde{I}_N^k$ images do not have to be saved. However, this may slow down the tracking. If all the effective images have been saved, this treatment can be done at the end since it is easily parallelizable.

2.6 Link between fringe position and evaporation

Wu [19] showed that as the droplet evaporates, its diameter decreases, and therefore the positions of the intensity maxima and minima change. Therefore from the position of the interference fringes, we will be able to discriminate whether the droplet evaporates or not. It is much simpler to estimate the beginning of evaporation from the position of the fringes than from the variation of the number of fringes as illustrated in figure 3.

The figure 3 illustrates the number and position of fringes over time (referenced by frame number). The position of the fringes is given by the phase from the Fast Fourier Transformation. A red band with a black line at its center highlights the position where the fringes start to move, so the evaporation starts.

The positioning of the beginning of the evaporation is done manually. This manual action ensures that the evaporation is well positioned and that the droplet is not a false positive and is followed up until the evaporation process is over. The positioning of the beginning of evaporation is done so that the red band, of a width of 6 frames on the figure 3, contains the center of this band gives the break of slope, the beginning of evaporation.

2.7 Fast evaporation

In some cases, the evaporation rate is so fast that it is no longer possible to measure the number of fringes. According to Wu et al.[19] it is possible to measure a nanoscale change in diameter from the displacement of the interference fringes. He proposes the following formula:

$$\Delta D = \Delta\theta \frac{\lambda}{2\pi} \left(\sin\left(\frac{\phi}{2}\right) + \sqrt{n^2 + 1 - 2n\cos\left(\frac{\phi}{2}\right)} \right)^{-1} \tag{2}$$

with θ the phase associated with the spatial frequency of the fringes.

If the evaporation process is too fast, the droplet's image is blurred, so the droplet's physical size cannot be tracked during evaporation. The end of this section estimates the speed evaporation process in case of burnt gas and links it to the fringe position.

We can assume that a shift of the order of π of the fringes, i.e., when the maxima shift to the minima during the exposure of the camera, makes it impossible to distinguish the interference fringes.

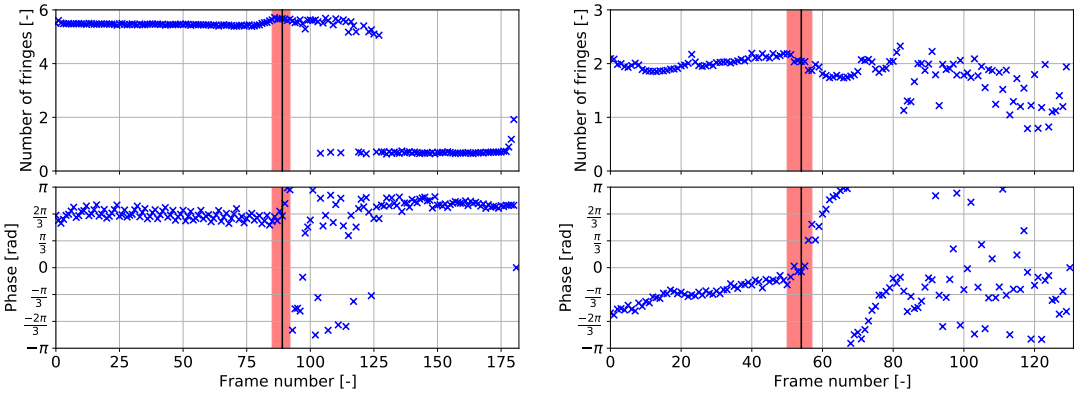

(a) Example with many fringes.

(b) Example with few fringes.

Fig. 3: Example of the evolution of the number of fringes and the phase of the maximum FFT. A red band with a black line at its center shows where the evaporation starts.

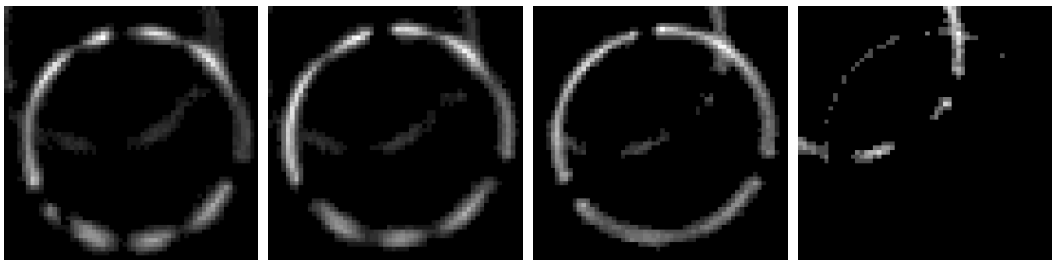

(a) $t = 0\,\mathrm{ms}$ (b) $t = 1.35\,\mathrm{ms}$ (c) $t = 2.7\,\mathrm{ms}$ (d) $t = 4\,\mathrm{ms}$

Fig. 4: Image of an evaporating droplet

Let's anticipate the orders of magnitude of the experiment presented below to evaluate what is a fast evaporation. For a shift of π we have in the experiment $\Delta D = 0.22\,\mu\mathrm{m}$. The evaporation rate of dodecane at 1730 K was measured by Muelas et al.[1] at $0.5348\,\mathrm{mm^2\,s^{-1}}$, based on the evolution of the diameter. Then for a $21.0\,\mu\mathrm{m}$ droplet, when half the mass is evaporated, the averaged speed of regression of its diameter is $16\,\mu\mathrm{m\,ms^{-1}}$, assuming that the surface of the droplet decrease linearly with time. This means that if the exposure of the camera exceeds $14\,\mu\mathrm{s}$, the fringes will be blurred.

To illustrate the above calculations, the image of a droplet during its evaporation phase is presented in figure 4. This $20\,\mu\mathrm{m}$ droplet evaporates over 4 ms. First, we can see that the fringes are visible on both the *a* and *b* images, although it seems that on the *b* image, the fringes are less clear because they move during the camera exposure. However, on the image *c*, it is no longer possible to distinguish the fringes and thus to hope to count them. This image illustrates the blurred droplet's image in case of *fast* evaporation. Finally, the image *d* shows a typical image of a droplet at the end of its life. The droplet is barely visible.

3 Experimental setup

3.1 Burner and optical diagnostics

The experimental setup chosen to apply the PTV diagnostic is the counterflow configuration (figure 5). A mixture of air and methane is injected from the bottom at an equivalence ratio of 0.9 with a Reynolds number of 1430 through a burner of 20 mm diameter. The top burner, similar to the bottom burner, injects air at Re = 950 containing a small amount of dodecane droplet ($6\,\mathrm{mg\,s^{-1}}$) so that the droplets evaporate on the hot front generated by the flame without disturbing the flow. The dodecane is injected by an ultrasonic injector fed by air and a syringe. The distance between the two burners is 52 mm. This configuration is protected by nitrogen co-flow.

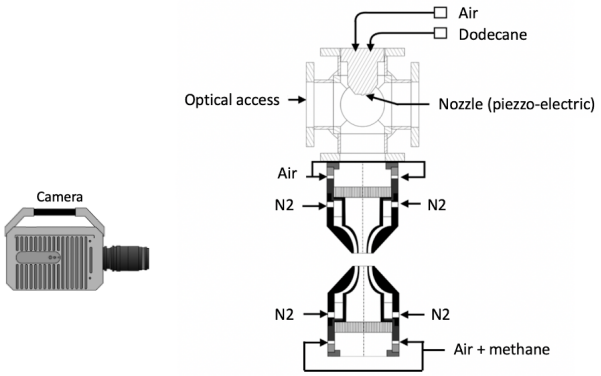

Fig. 5: Schematic representation of the experimental setup.

In order to carry out the diagnosis, a laser sheet centered on the burner axis and with a width of 1 mm is emitted from a Continuous Wave (CW), frequency-doubled Nd:YAG laser (Verdi G) operating at the wavelength of 532 nm and a cylindrical lens. A camera, placed at a forward scattering angle of 60°, acquires the images of the droplets at 20 kHz with a resolution of 720×504 pixels and an exposure time of 50 µs. The camera is equipped with a Nikkon 105 mm AF-DC lens and a 24 mm extension ring, allowing to obtain a defocused image of the droplets. Moreover, a special mask, presented above, was installed in the extension ring to modify the droplets' image. According to Damaschke et al.[16], $D = \kappa N_f$ (for details see Eq 1), where D is the physical size of the droplet, N_f the number of fringes and κ the proportionality factor. In this experimental setup, $\kappa = 4.9\,\mu m$.

3.2 Characterization of the velocity and temperature field

In order to fully characterize the experimental setup, the 2D velocity and the temperature field in the laser sheet are measured. These fields were measured without droplets since they would have interfered with the techniques used. The camera is placed at a 90° forward scattering angle for both measurements.

3.2.1 Velocity field measurement

The velocity field shown in figure 6 was obtained by PIV measurement. Oil droplets of a few microns are injected into the top burner. These droplets are small enough to assume that their speed is identical to the flow. A double pulsed Nd:YAG laser with a 532 nm generates a laser sheet similar to the one used for the PTV to illuminate the droplets. Images are acquired with a 2048×2048 pixels camera and processed with Dantec Dynamics Studio. These droplets evaporate at a temperature of 500 K, the end of the velocity field measurable by this technique shows this isotherm.

This isotherm was followed to determine the stability of the hot front and oscillates over a range of 0.5 millimeter around a stable position. This oscillation is slightly asymmetric, with a slightly larger fluctuation for positive horizontal positions.

3.2.2 Temperature field measurement

The temperature field is measured by Rayleigh method [28]. A laser with 532 nm excites the gaseous molecules in the burner, and an intensified camera, placed perpendicularly to the laser sheet, acquires this signal. The signal intensity depends on the density and composition of gas within the laser sheet.

The density decreases when the temperature increases, and the Rayleigh intensity decreases because it is proportional to the number of molecules in the laser beam. From the diminution

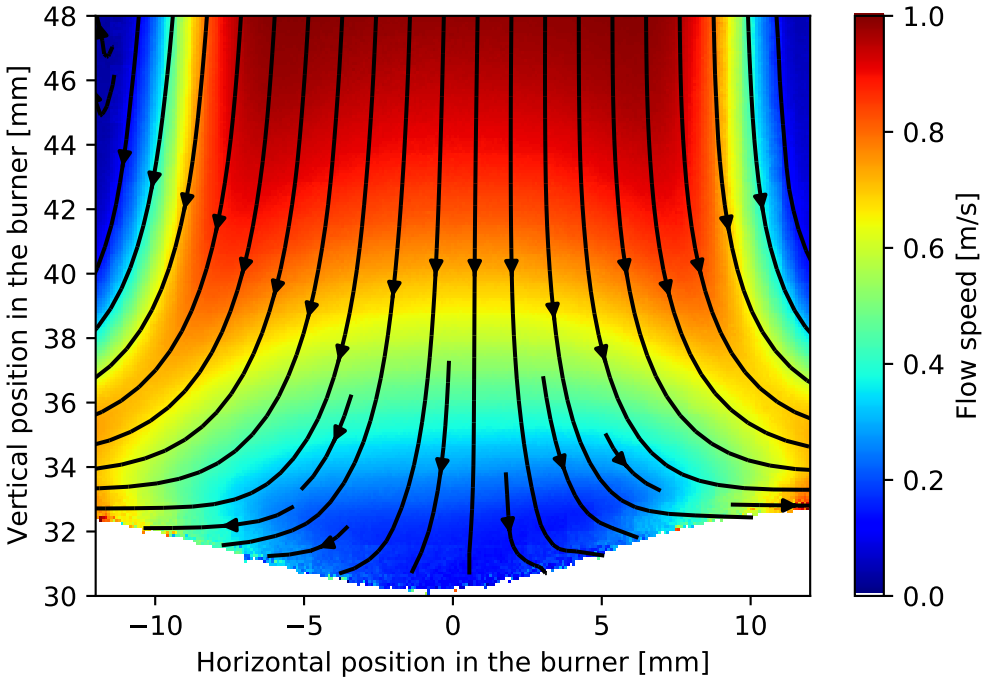

Fig. 6: 2D velocity map measured by PIV

of the Rayleigh signal, the burnt gas temperature can be measured. However, the composition is slightly different, and taking into account the presence of CO_2, CO and H_2O in the burnt gas, one can estimate that the signal ratio at the same temperature between the cold and burnt gas is 1.09.

In order to estimate the temperature in the burnt gas region and the cold gas region, the laser beam has been focused toward these regions and the temperature was estimated from the signal intensity.

The fresh gas temperature, measured by the thermocouple, is 317 K. From the Rayleigh signal, we can estimate the temperature ratio between fresh and burnt gas. Finally, the burnt gas temperature is 1935 K with an uncertainty of the order of 50 K.

Then, from the local measurement, a 2D field of the temperature is measured in 3 steps :

1. A temperature field is determined by assuming that all gas has the same composition as fresh gas
2. From this field and assuming a unitary Lewis number, the 2D mixing field between fresh and burnt gases is determined
3. Thanks to this field of composition, a local temperature correction coefficient is evaluated

The correction is minor, and the uncertainty high; it is not necessary to make several loops to obtain the result, mainly since this correction only affects the temperature gradient zone.

The resulting temperature field is shown in figure 7. The signal being very noisy, a low pass median filter was applied to reconstruct the temperature field with a spatial cutoff frequency of 0.6 mm.

We can see the shape of the warm front is similar to the shape of the isotherm obtained by measuring the velocity field in figure 7, with however a vertical shift of about 4 mm for the 500 K isotherm.

3.2.3 Temperature and velocity profile along the burner axis

The position of the hot front in the Rayleigh measurement, PIV measurement, and PTV measurements on the droplet is not strictly the same. This variation is caused by environmental factors that affect the position of the front between two experiments, despite using similar conditions. No evident variations were observed within one experimental campaign. Thus, we had to make

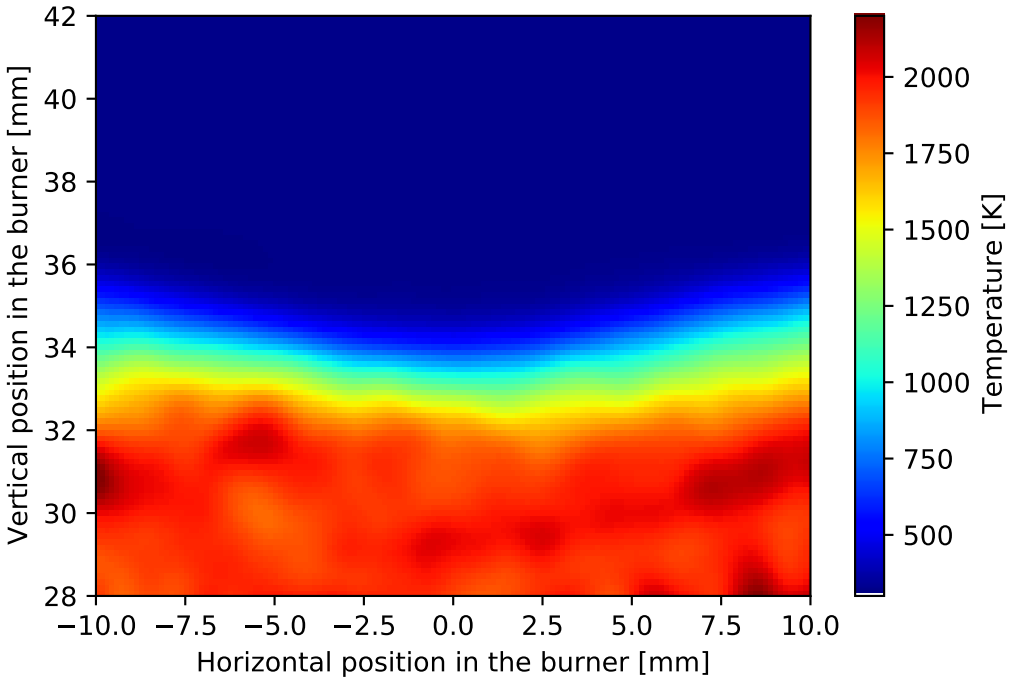

Fig. 7: 2D temperature map reconstructed from the Rayleigh signal

sure that the front was stabilized during each measurement to be comparable, as no simultaneous measurements could be performed. The difference in position will mainly impact the flow away from the axis of symmetry, so the velocity and temperature field measured away from the axis of symmetry do not represent the environmental conditions that the droplets experienced. However, we can estimate that the velocity and temperature conditions near the axis depend little on the position of the hot front as long as it remains far enough from the burner edges (which is the case for each of our measurements). Thus we estimated the shift for each case, taking the PTV as a reference.

To position the gas velocity field with respect to the droplet velocity, we compared the instantaneous velocity of droplets smaller than 20µm and within 2mm off the axis of symmetry. These droplets have a Stokes number smaller than 0.025, so they have a velocity almost identical to air. Thanks to the 750 instantaneous velocities collected from droplets verifying the indicated conditions and the least squares method, we estimate an average vertical shift equal to 9.40 mm($\pm$0.01 mm) between the PIV and the PTV measurement.

We used the boiling point of the oil droplets used for PIV to reposition the temperature measurement. Since they evaporate at 500K, the velocity field can be positioned relative to the temperature field. We estimate that the vertical shift between the temperature and the PTV measurement is 12.55 mm($\pm$0.01 mm). Those vertical shifts correspond to mean changes of the stabilization point. Finally, the temperature and velocity profile along the axis of symmetry has been drawn on the same graph (see figure 8).

4 Experimental results

4.1 Droplet selection process

Following the 20,000 processed images of evaporating droplets, 105 droplets are retained among all. More droplets were found, but a part of them was rejected for the following reasons:

- Not visible on more than 100 consecutive images
- Impossible to clearly identify the evaporation phase
- Clear break in the intensity of the droplets

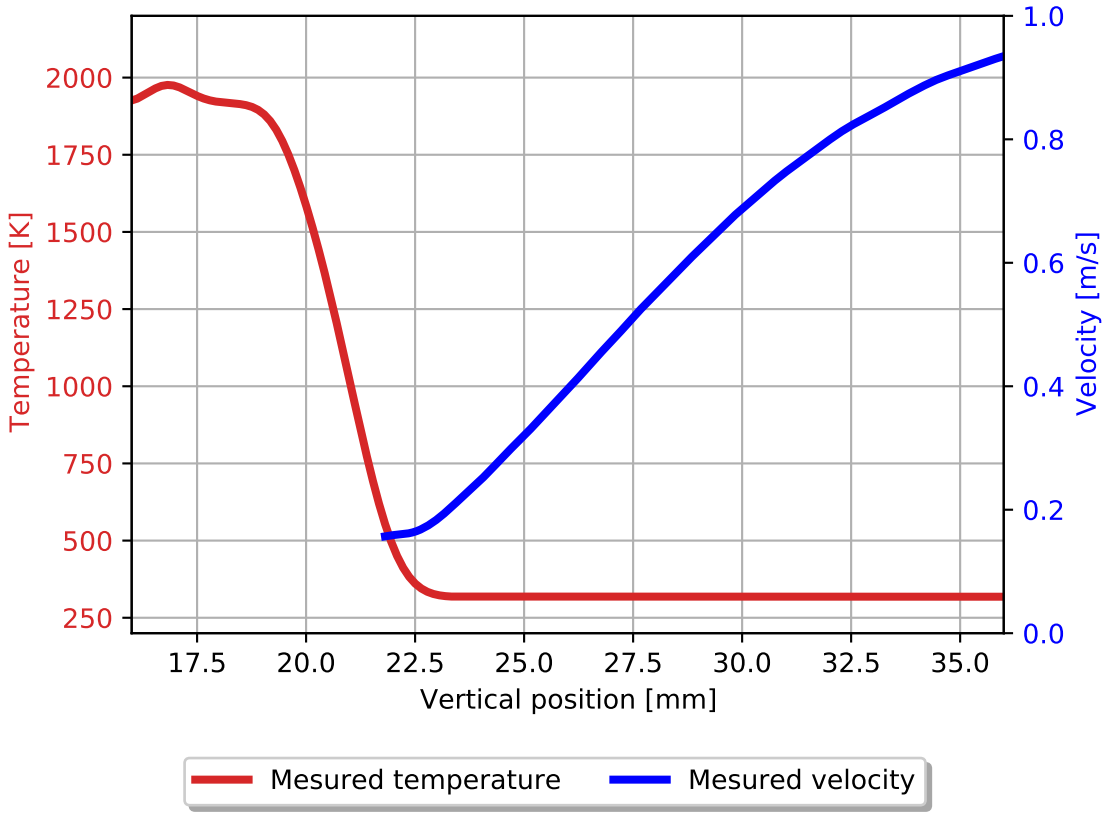

Fig. 8: Velocity and temperature along the burner axis.

The purpose of these criteria is to select the droplets that evaporate into the laser sheet.

The majority of the measured droplets are tracked over approximately 300 images. In addition, each selected droplet is manually checked to ensure that the tracking is correct.

The clear break in the intensity criteria stands for droplets leaving the laser sheet. Most of the droplets rejected for this criteria have, in the worst case, barely started their evaporation before disappearing.

4.2 Sizes and trajectories obtained by the presented PTV algorithm

Figure 9 shows the trajectory of 10 droplets selected among the 105 droplets to illustrate the typical trajectories obtained by PTV. The measured trajectories match the expected ones in this configuration [29], as well as for the evaporation location.

The uncertainty on the initial time of evaporation is 0.15 ms as shown in figure 3 since this moment is positioned with 3 frames uncertainties and the sampling rate is 20 kHz. We found that the light intensity of the droplets on the camera decreases linearly with time during the last frames. We used this observation to estimate the end time of evaporation. We made a linear interpolation from the last 20 frames to estimate the moment when the intensity is zero, and the droplet will have disappeared. The end of evaporation with this method is almost the same as the vanishing of the droplets from the frames with an average discrepancy of 0.15 ms. Overall, the total evaporation delay uncertainty is estimated at 0.3 ms.

Figure 10 shows the distribution of initial droplet diameter and suggests that the method does not favor any droplet size. The Sauter mean diameter is 21.0 µm, and the diameter uncertainty is 2 µm from work done on the effect of burnt gases.

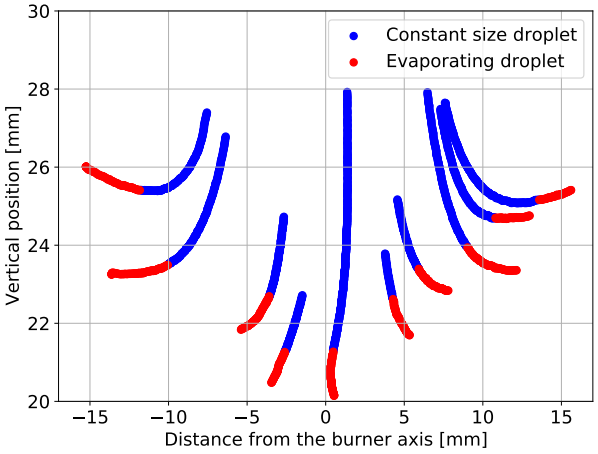

Fig. 9: 10 droplets' trajectory

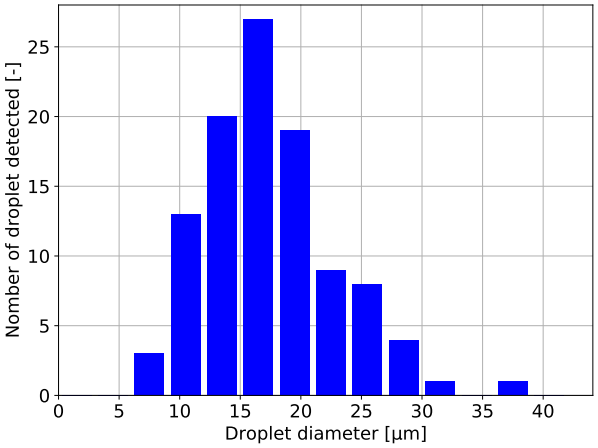

Fig. 10: Distribution of the initial droplets' diameter

4.3 Relevance of the algorithm compared to a classical PTV algorithm

A classical PTV algorithm is done in two steps: First, it *detects* the droplets on the set of images, then from the *detected* droplets, it recreates trajectories. In the case of the present work, it means that the trajectories would be determined from the set of F_N. Even with the best matching algorithm, the only trajectories that could be done would come from the set F_N. However, in the present work, the trajectories are reconstructed from the set D_N since a step of *follow-up* has been introduced.

For non-evaporating droplets, only 25 % of the followed droplets positions are not detected. Then a good matching algorithm would have found almost as many trajectories as our algorithm during this phase. However, for evaporation droplets, 65% of the followed droplets positions are not detected, and it rises up to 91% during the last millisecond (20 last points of the red part of the trajectories in the figure 9). So, even with a good matching algorithm, it would have been tough to recreate the trajectories for evaporation droplets. Thus, relying only on the detected droplets, it is impossible to correctly follow the evaporating droplets.

This shows the interest of the *followed-up* phase and what this phase brings in the case of droplets with a significant difference of intensity and some of which are almost entirely evaporated.

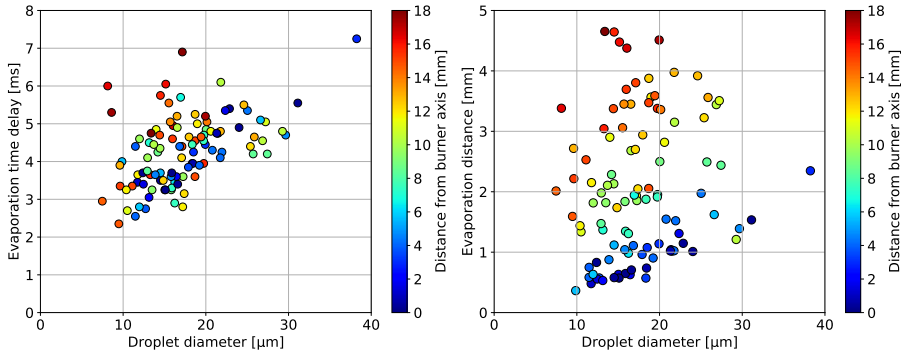

(a) Characteristic evaporation time delay (b) Evaporation characteristic distance

Fig. 11: Data collected during the measurement campaign. Each point represents a droplet and these are colored by their mean distance from the burner axis during their evaporation phase.

4.4 Characteristic evaporation time

Evaporation is measured as the time spent between the beginning of evaporation and the vanishing of the droplets. The figure 11 shows the evaporation time of the droplets as a function of their initial diameter.

The order of magnitude related to the evaporation delay is consistent with the estimation in part 3. The delay is slightly larger because the droplets start to evaporate before entering the burnt gas and therefore evaporate at a lower average temperature. The larger droplets evaporate more slowly because they are heavier, which explains the increase of the overall evaporation delay with the diameter of the droplets.

A dispersion in evaporation delay is observed. This dispersion is larger than the uncertainty on the evaporation time of the droplets. The dispersion may be due to the slight instability of the heat front. Nevertheless, the reader must keep in mind that the real temperature and velocity field are unknown for droplets far from the burner central axis. These fields could not be measured because the measurement was not possible with droplets.

4.5 Evaporation characteristic distance

As the droplets are followed during their evaporation phase, the distance they evaporate is also measured. The evaporation distance as a function of the initial diameter of the droplets is plotted in figure 11.

As for the evaporation time, dispersion on the evaporation distance can be observed. The dispersion is related to the mean distance from the burner axis during the evaporation process. When the size of the droplets is fixed, a greater distance to the burner axis leads to a greater evaporation distance. Indeed, the more the droplet is far from the axis, the more significant the horizontal flow and the drag force are. Thus, this increases the evaporation distance since the droplets are carried by the horizontal flow over a more significant distance.

The evaporation distance increases with the diameter of the droplets at a given mean distance from the burner axis. Bigger droplets take more time to evaporate and travel a greater distance. Moreover, these droplets being initially more significant, they have greater inertia and thus have a greater speed during the evaporation phase.

5 Measurements with the bottom burner offset from the top burner to evaluate the effect of the burnt gases

5.1 Measurement setup and methodology

Burnt gas is present on the optical path between the droplets and the camera. This part assesses the effect of the burnt gas on the image of the droplets.

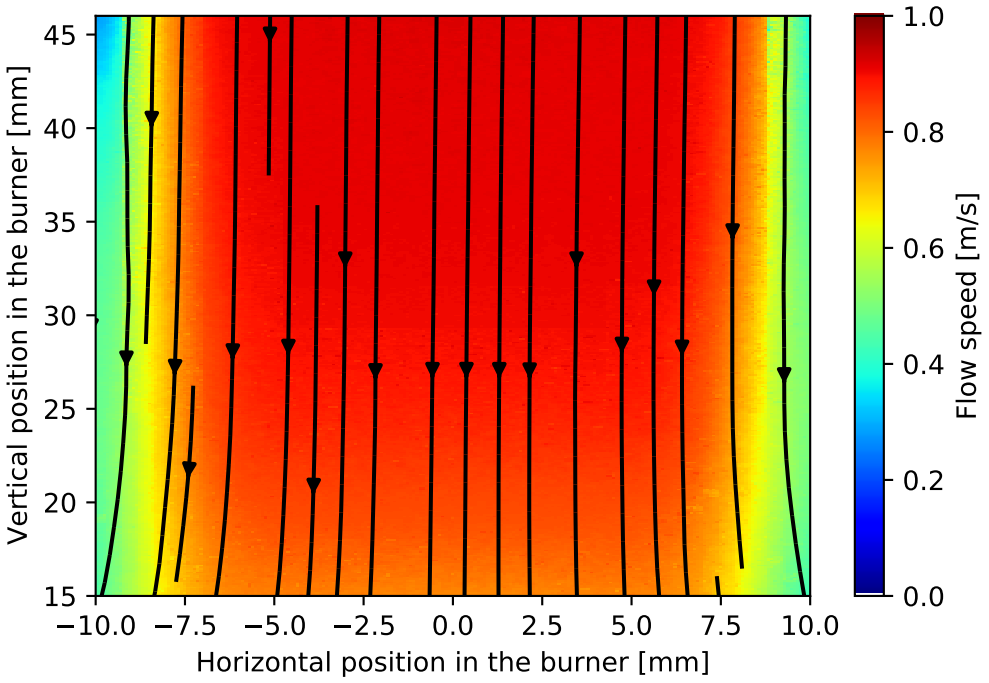

Fig. 12: Velocity map for the offset burner configuration.

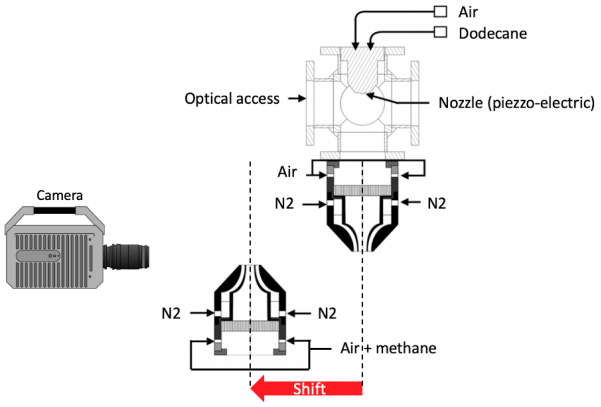

Fig. 13: Scheme of the offset burner configuration.

The setup selected for this purpose is the same as above but with the bottom burner mid-distance between the top burner and the camera. This configuration is presented in figure 13, with a distance between the camera and the top burner of about 30 cm and of 15 cm for the bottom burner. There is burnt gas on the optical path between the droplets and the camera in this setup without affecting the droplets.

The velocity field of this configuration is measured by PIV and is presented in figure 12. Let us estimate the accuracy of the PTV measurement by assuming that the droplets have a constant velocity and diameter because they are only carried in a vertical flow at room temperature. In this configuration, 3000 images were acquired with the bottom burner turned off and 3000 images with the burner turned on.

The objective is to determine the deviation of the horizontal and vertical position as well as the position and number of fringes with respect to the assumptions made above. The parameters of the PTV algorithm are identical as for the case of evaporating droplets with the burners facing each other.

	Without flame	With flame
Horizontal position [pixel]	0.119 (20193)	0.0922 (17537)
Vertical position [pixel]	0.116 (20193)	0.105 (17537)
Fringes number [-]	0.135 (9374)	0.227 (9413)
Phase [rad]	0.312 (9374)	0.375 (9413)

Table 1: Dispersion of the measured values in the offset burner configuration. The number of position used for the statistics are between brackets.

5.2 Data collected during the measurement

When the bottom burner is turned off, the algorithm found 85 droplets; 68 were actual droplets. In contrast to the measure where the droplets evaporate, there are slightly more false positives, here 20%. In this setup, the top burner is not heated by the flame. This low temperature increases the number of droplets that reach the measurement area because they do not evaporate on the way. Thus, this high density of droplets generates a greater quantity of false positives. These 68 droplets are used to determine the uncertainty of measurement on the position of the droplets. Among these 68 droplets, there are 58 for which it is possible to measure the diameter during at least 50 consecutive images correctly. We use the images where it is possible to measure the number of fringes to estimate the accuracy of the position and the number of fringes. The SMD of these droplets is 17.1 µm.

When the bottom burner is lit, 88 droplets are found with 65 exploitable trajectories. Moreover, among these exploitable trajectories, it is possible to measure the number and the position of fringes on 44 of these droplets. The SMD of the droplets thus obtained is 16.6 µm. This allows us to see that the data obtained are comparable and that the same quantity is measured in both cases. The burnt gases do not significantly affect the amount of data acquired.

5.3 Limit of the measurement

The dispersion of the measurements with respect to the previously stated hypotheses is presented in the table 1. In this table, the number of points that allowed to determine this standard deviation is specified between brackets:

We can see that the accuracy of the trajectory is not affected by the burnt gases. The uncertainty remains around 0.1 pixels. Indeed, the effect of the burnt gases generates fluctuations with characteristic times more significant than the sampling time, and therefore, the trajectory remains globally stable.

On the other hand, the burnt gases affect the interference signal, and therefore the accuracy of the number and position of the fringes decreases. When the burnt gases disturb the droplet's signal, its image is distorted, so it is more difficult to measure its size and extract the signal from the fringes. Nevertheless, the extrema remain correctly positionable, which explains why the effect on the phase is less significant than on the fringes.

6 Conclusion

The present work introduced a new PTV algorithm to measure evaporation time delay and length of droplets evaporating droplets in the vicinity of a flame. It adapted ILIDS measurement with a high-frequency PTV tracking to follow the evaporation of droplets.

The beginning of the evaporation process was determined from the nanoscale change in diameter of the droplets obtained from the position of the fringes. Then during the evaporation, ILIDS was no longer possible since fringes are not stable enough, and so it was not possible to estimate the evaporation delay from the droplets' diameter decrease. However, this delay was measured thanks to the new PTV algorithm since the droplets were followed during their whole evaporation process.

Thus, in addition to the information on the number of fringes, their position has been exploited to determine the beginning of the evaporation process. Measuring the evaporation from allows to estimate the beginning of the evaporation more simply than by looking at the decrease of the number of fringes. Moreover, it is challenging to follow the evolution of the number of fringes during

the evaporation process because they are not fixed during the camera exposure. Nevertheless, the effect of the environment could be evaluated, particularly the effect of the burnt gases, and it could be shown that the dispersion of the measured quantities remains very reasonable.

Finally, the length and the characteristic time of evaporation could be measured. A significant dispersion of the evaporation lengths could be observed, but it seems that this can be explained in large part by the eccentricity of the droplets.

Thanks to this new technique, it will be possible to measure and observe new phenomena thanks to this Lagrangian tracking of fuel droplets.

References

1. Á. Muelas, J. Carpio, J. Ballester, A. L. Sánchez, and F. A. Williams, "Pyrolysis effects during high-temperature vaporization of alkane droplets," *Combustion and Flame*, vol. 217, pp. 38–47, July 2020.
2. W. Shang, S. Yang, T. Xuan, Z. He, and J. Cao, "Experimental studies on combustion and microexplosion characteristics of n-alkane droplets," *Energy & Fuels*, vol. 34, pp. 16613–16623, Nov. 2020.
3. C. Chauveau, F. Halter, A. Lalonde, and I. Gökalp, "An experimental study on the droplet vaporization: effects of heat conduction through the support fiber. it 2008," 01 2008.
4. H. Nomura, Y. Ujiie, H. J. Rath, J. Sato, and M. Kono, "Experimental study on high-pressure droplet evaporation using microgravity conditions," *Symposium (International) on Combustion*, vol. 26, pp. 1267–1273, Jan. 1996.
5. H. Ghassemi, S. W. Baek, and Q. S. Khan, "Experimental study on evaporation of kerosene droplets at elevated pressures and temperatures," *Combustion Science and Technology*, vol. 178, pp. 1669–1684, Aug. 2006.
6. M. Stöhr, S. Ruoff, B. Rauch, W. Meier, and P. L. Clercq, "Droplet vaporization for conventional and alternative jet fuels at realistic temperature conditions: Systematic measurements and numerical modeling," *Proceedings of the Combustion Institute*, vol. 38, no. 2, pp. 3269–3276, 2021.
7. Y. Wu, C. Crua, H. Li, S. Saengkaew, L. Mädler, X. Wu, and G. Gréhan, "Simultaneous measurement of monocomponent droplet temperature/refractive index, size and evaporation rate with phase rainbow refractometry," *Journal of Quantitative Spectroscopy and Radiative Transfer*, vol. 214, pp. 146–157, 2018.
8. Y. Wu, H. Li, X. Wu, G. Gréhan, L. Mädler, and C. Crua, "Change of evaporation rate of single monocomponent droplet with temperature using time-resolved phase rainbow refractometry," *Proceedings of the Combustion Institute*, vol. 37, no. 3, pp. 3211–3218, 2019.
9. C. Li, Q. Lv, Y. Wu, X. Wu, and C. Tropea, "Measurement of transient evaporation of an ethanol droplet stream with phase rainbow refractometry and high-speed microscopic shadowgraphy," *International Journal of Heat and Mass Transfer*, vol. 146, p. 118843, 2020.
10. L. Perrin, G. Castanet, and F. Lemoine, "Characterization of the evaporation of interacting droplets using combined optical techniques," *Experiments in Fluids*, vol. 56, Jan 2015.
11. G. König, K. Anders, and A. Frohn, "A new light-scattering technique to measure the diameter of periodically generated moving droplets," *Journal of Aerosol Science*, vol. 17, no. 2, pp. 157–167, 1986.
12. R. Ragucci, A. Cavaliere, and P. Massoli, "Drop Sizing by Laser Light Scattring Exploiting Intensity Angular Oscillation in the mie regime," *Particle Particle Systems Characterization*, vol. 7, no. 1-4, pp. 221–225, 1990.
13. M. Maeda, T. Kawaguchi, and K. Hishida, "Novel interferometric measurement of size and velocity distributions of spherical particles in fluid flows," *Measurement Science and Technology*, vol. 11, no. 12, 2000.
14. M. Maeda, Y. Akasaka, and T. Kawaguchi, "Improvements of the interferometric technique for simultaneous measurement of droplet size and velocity vector field and its application to a transient spray," *Experiments in Fluids*, vol. 33, no. 1, pp. 125–134, 2002.
15. Y. Hardalupas, S. Sahu, A. M. Taylor, and K. Zarogoulidis, "Simultaneous planar measurement of droplet velocity and size with gas phase velocities in a spray by combined ILIDS and PIV techniques," *Experiments in Fluids*, vol. 49, no. 2, pp. 417–434, 2010.
16. N. Damaschke, H. Nobach, T. I. Nonn, N. Semidetnov, and C. Tropea, "Multi-dimensional particle sizing techniques," *Experiments in Fluids*, vol. 39, pp. 336–350, June 2005.
17. Y. Park, G. Choi, and L. Zimmer, "Experimental study of the dynamics of pulsated laminar counter-flow spray flames using optical flow and proper orthogonal decomposition," *The Proceedings of the International symposium on diagnostics and modeling of combustion in internal combustion engines*, vol. 2017.9, no. 0, p. C107, 2017.
18. R. Thimothée, C. Chauveau, F. Halter, and I. Gökalp, "Experimental investigation of the passage of fuel droplets through a spherical two-phase flame," *Proceedings of the Combustion Institute*, vol. 36, no. 2, pp. 2549–2557, 2017.
19. Y. Wu, H. Li, M. Brunel, J. Chen, G. Gréhan, and L. Mädler, "Phase interferometric particle imaging for simultaneous measurements of evaporating micron-sized droplet and nanoscale size changes," *Applied Physics Letters*, vol. 111, no. 4, p. 041905, 2017.
20. H. G. Maas, A. Gruen, and D. Papantoniou, "Particle tracking velocimetry in three-dimensional flows - Part 1. Photogrammetric determination of particle coordinates," *Experiments in Fluids*, vol. 15, no. 2, pp. 133–146, 1993.
21. L. Qieni, H. Kan, G. Baozhen, and W. Xiang, "High-accuracy simultaneous measurement of particle size and location using interferometric out-of-focus imaging," *Optics Express*, vol. 24, no. 15, p. 16530, 2016.
22. M. G. Jeon, D. H. Doh, and G. R. Cho, "Development of interpolation-free PTV," *Journal of Mechanical Science and Technology*, vol. 35, no. 9, pp. 4023–4032, 2021.
23. K. Liu and D. Liu, "Particle tracking velocimetry and flame front detection techniques on commercial aircraft debris striking events," *Journal of Visualization*, vol. 22, no. 4, pp. 783–794, 2019.

24. A. Quérel, P. Lemaitre, M. Brunel, E. Porcheron, and G. Gréhan, "Real-time global interferometric laser imaging for the droplet sizing (ilids) algorithm for airborne research," *Measurement Science and Technology*, vol. 21, Dec 2009.
25. S. J. Lee, E. Kawakami, and R. E. Arndt, "Application of a shadow image velocimetry to a ventilated hydrofoil wake," *Journal of Visualization*, vol. 17, no. 4, pp. 327–335, 2014.
26. R. Baudoin and L. Zimmer, "Procédé et système optique de détection de particules dans un écoulement," 12/2015. FR Patent 13 61580.
27. M. Guizar-Sicairos, S. T. Thurman, and J. R. Fienup, "Efficient subpixel image registration algorithms," *Optics Letters*, vol. 33, no. 2, p. 156, 2008.
28. A. R. Masri, R. W. Dibble, and R. S. Barlow, "The structure of turbulent nonpremixed flames revealed by Raman-Rayleigh-Lif measurements," *Progress in Energy and Combustion Science*, vol. 22, no. 4, pp. 307–362, 1996.
29. A. Liñán, D. Martínez-Ruiz, A. L. Sánchez, and J. Urzay, "Regimes of spray vaporization and combustion in counterflow configurations," *Combustion Science and Technology*, vol. 187, no. 1-2, pp. 103–131, 2015.